Materials Advances

ROYAL SOCIETY
OF CHEMISTRY

PAPER
Tae-Hyuk Kwon, Pooi See Lee *et al*.
From black pigment to green energy: shedding light on
melanin electrochemistry in dye-sensitized solar cells

PAPER

From black pigment to green energy: shedding light on melanin electrochemistry in dye-sensitized solar cells†

Noah Al-Shamery, [iD] ‡[a] Jun-Hyeok Park, [iD] ‡[b] Seung Rok Kim, [iD] ‡[b] Florian Heppner, [iD] [c] So Yeon Yoon, [iD] [b] Thomas Bredow,[c] Tae-Hyuk Kwon [iD] *[b] and Pooi See Lee [iD] *[a]

The sustainably obtainable poly indolequinone eumelanin shows exciting properties for green, natural dye sensitized solar cell (DSSC) applications: broad absorption until 800 nm, metal ion chelation, and long conjugated, aromatic structures featuring an abundance of quinone, semiquinone, and some hydroquinone moieties providing rich binding sites. Despite this, there are limited literature works covering the use of this natural dye that typically reported conversion efficiencies of less than 0.10%. Thus, there is room for improving both the performance and understanding of the electrochemical mechanisms behind eumelanin-based DSSC applications. This work fills this gap by first characterizing eumelanin to confirm its potential stability in films on TiO_2 substrates, then providing theoretical calculations on the HOMO−LUMO gap and simulating the absorption spectrum, giving promising results for potential use as a dye in DSSCs, and finally covering new ground in the optimization of the fabrication process of eumelanin-sensitized DSSCs. The prepared eumelanin DSSC devices are of high cycling stability and show a maximum performance of 0.24% before and 0.42% after treatment with UV-light. The devices were analyzed in detail to give insights into the microscopic explanation of why eumelanin-based DSSCs differ from other natural dye-based devices. Using intensity modulated photocurrent and photovoltage spectroscopy, the comparatively high recombination rate of eumelanin in relation to other natural dyes is identified as the main inhibitor to overcome in future endeavors of optimizing eumelanin films in DSSCs.

[a] School of Materials Science and Engineering, Nanyang Technological University, 50 Nanyang Ave, Singapore, 639798, Singapore. E-mail: pslee@ntu.edu.sg

[b] Department of Chemistry, Ulsan National Institute of Science and Technology, Ulsan, 44919, Republic of Korea. E-mail: kwon90@unist.ac.kr

[c] Mulliken Center for Theoretical Chemistry, University of Bonn, D-53115, Germany

† Electronic supplementary information (ESI) available: Further detailed experimental descriptions; summarized DSSC performance data of relevant literature devices; photovoltaic parameters for melanin-DSSCs with different redox mediators; light harvesting efficiency of melanin thin-films compared to melanin dissolved in a DMSO/MeOH solution (1:19); photos of bare TiO_2/melanin-sensitized TiO_2 photoanodes; bode plot of the recorded electrochemical impedance data of the melanin-based DSSC devices; graphical scheme of the difference in recombination kinetics between melanin and other dyes used in DSSC set-ups; photographs of the prepared DSSC devices using melanin as the dye discussed in this work; unmodified, complete simulated absorption spectrum of a gas-phase melanin tetramer in the "6 H structure" calculated using MOLGW at the BhLYP/cc-pVDZ(-RI) level of theory (PDF). See DOI: https://doi.org/10.1039/d5ma00081e

‡ Noah Al-Shamery, Jun-Hyeok Park, and Seung Rok Kim have contributed equally to this work and share co-first authorship.

Introduction

The biological pigment melanin is well-known for qualities inside the human body like photoprotection, radical scavenging, and metal ion chelation that can be interesting for applications in materials science. Depending on the structure of the molecule consisting of different molecular building blocks, melanin is classified into several sub-classes like pheomelanin, allomelanin, neuromelanin, and eumelanin.[1,2] Specifically the poly indolequinone eumelanin, just called "melanin" in the following, has recently gained increased interest for electrochemical applications due to its polydopamine-like structure, making it one of the most well-characterized pigments.[3–5] Santato *et al.* have shown that the material shows promise in organic solar cell applications due to the possibility of exploiting the quinone/hydroquinone equilibrium and metal ion chelation capabilities of the molecule.[6]

The structure of melanin consisting of the monomers 5,6-dihydroxyindole-2-carboxylic acid (DHICA) and 5,6-dihydroxy-indole (DHI) that are present in either the hydroquinone,
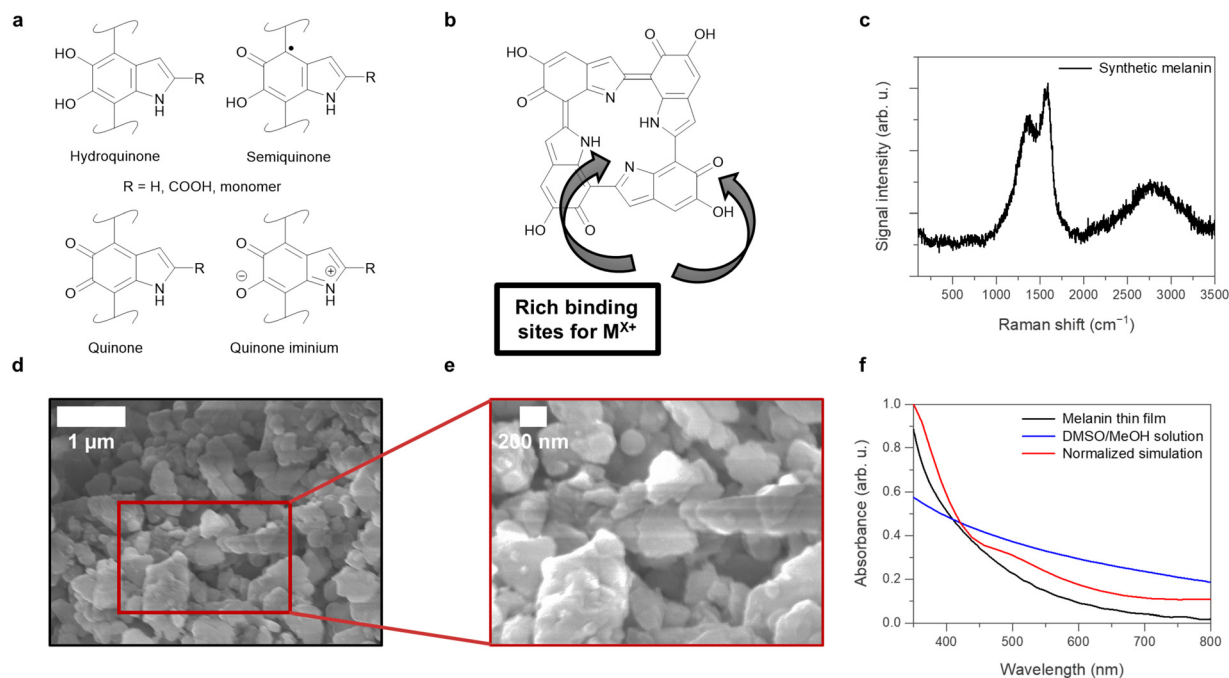
Fig. 1 Redox states of melanin monomers (a) and locations of potential binding sites in a selected melanin tetramer (b). (c) The Raman spectroscopy data of synthetic melanin bulk powder, and (d) and (e) scanning electron microscopy images of sonicated synthetic melanin drop-cast on a Si wafer using 5.0 kV as accelerating voltage (secondary electron imaging). (f) A comparison of normalized UV-visible (UV-vis)-absorption spectra of melanin in thin-films, solutions, and the simulated spectrum of a gas-phase melanin tetramer using MOLGW on the BHLYP/cc-pVDZ(-RI) level of theory.

semiquinone, quinone, or quinone iminium form, can be seen in Fig. 1(a) together with the oligomeric tetramer structure that is considered to be one of the potential energetic minimum structures of the polymer in Fig. 1(b). Another potential unit of interest is the ionized form of the quinone methide at alkaline and neutral pH values as discussed in various literature.[7-9] Besides the tetramer structures that can self-assemble *via* π-π-stacking and solvophobic effects,[10] the disordered melanin units are theorized to also exist in bulk as dimers, larger oligomers, and chain structures, depending on the synthesis conditions or source of extraction.[11,12] The energy storage capabilities of the melanin stem from both the redox equilibrium between the depicted redox states, and the comproportionation reaction of quinone and hydroquinone units.[13] Melanin consisting of conjugated DHICA and DHI monomers shows an absorption range from 400 nm to 800 nm. The absorbed light produces the excited state of the melanin structure, leading to heat (photothermal effect) and/or, light emission (photoluminescence), or charge extraction through external electron transporting (photovoltaic effect);[14] for instance, they have been utilized in light-to-heat conversion applications in combination with materials like graphene oxide (GO) and perovskites.[14-16] Light-activation has also been suspected to shift the melanin comproportionation equilibrium to the production of semiquinone radicals, which has been linked to the biologically harmful photoreactivity and photoconductivity commonly associated with melanin.[17,18] Despite its potential for good solar light harvesting, there have been only few efforts found in the literature so far that try to utilize melanin

or melanin-like materials for harnessing light-to-electric conversion.[19,20]

To understand the light-to-electric conversion mechanism of melanin, its use as a sensitizer in dye-sensitized solar cells (DSSCs) is explored in this work.[21,22] For this application, melanin offers two advantages when compared to commonly used natural dyes such as anthocyanins or chlorophyll derivatives:[21,23,24] (1) its broad absorption range facilitates efficient light harvesting and electron excitation; and (2) the hydroquinone, semiquinone, and quinone moieties produced under oxidative conditions serve as binding sites for titanium dioxide (TiO$_2$), leading to the enhanced adsorption of melanin onto TiO$_2$ surfaces.[25-27] Prior research on melanin-DSSCs showed efficiencies below 0.1%, similar to devices using unsensitized TiO$_2$ alone.[28] The photoconversion mechanisms of melanin are yet to be elucidated fully (see Table S1 for a comparison of related reports, ESI†).[19,29] This study seeks to fill the critical gap in fundamental understanding and application of the light-to-electric conversion of melanin. In this work, the synthetic melanin is first characterized to assess its suitability for DSSC applications using spectroscopy to confirm the chemical stability and presence of rich binding sites. The film stability is evaluated using microscopic analysis. Computational methods are used to validate and support the viability assumptions by simulating the melanin absorption spectrum and giving the energies of the highest occupied molecular orbital (HOMO) and the lowest unoccupied molecular orbital (LUMO) of the electronic gap. Finally, the melanin-DSSCs were optimized and analyzed in detail to understand the electrochemical mechanisms,

photostability, and governing factors of melanin as a natural pigment dye in DSSCs.

Results and discussion

Viability of melanin in DSSCs

To confirm the viability of melanin as a natural dye in DSSCs, the potential interaction with TiO_2 was analyzed by confirming the chemical structure of the synthetic melanin using Raman spectroscopy. The surface morphology of the synthetic melanin was evaluated using scanning electron microscopy (SEM). The synthetic melanin analyzed was prepared by oxidation of tyrosine with hydrogen peroxide.[30] The results of the Raman spectroscopy measurements can be seen in Fig. 1(c). As expected for melanin, peaks around 1350 cm^{-1} and 1550 cm^{-1} can be observed. These peaks originate from the stretching mode of the aromatic C–N moiety and the aromatic C=C stretching vibrations in the melanin poly indolequinone structure.[31,32] Additionally, a weak shoulder peak around 1690 cm^{-1} is observed that correlates to quinone C=O stretching found in the indole quinone and semiquinone structures of melanin.[31] The broad peak around 2820 cm^{-1} can be attributed to the 2D band stemming from two-phonon double resonance Raman processes typically observed for aromatic carbon compounds.[33] This data correlates with previous literature observations, confirming both the chemical stability of the synthetic melanin and the presence of the quinone-moieties and porphyrin-like indole nitrogen atoms that can be beneficial for increasing the interaction with a TiO_2 substrate when using melanin as a dye in DSSCs.

As melanin has shown poor solubility in water and common polar organic solvents like acetone or benzene,[34] forming partial solutions/dispersions, it is important to consider the particle size of the material as well when deliberating the interaction with TiO_2. From the SEM pictures shown in Fig. 1(d) and the close-up depicted in Fig. 1(e), obtained from an investigation at high magnifications of a sample discussed in previous works covering the usage of melanin in multi-functional composites,[35] an average particle size of (202 ± 2) nm can be obtained. This matches previous findings for melanin. Because this size is larger than the size range average of TiO_2 particles ($\sim$20 nm), for the melanin interaction in DSSCs, it is expected that most likely only the dissolved, small-sized melanin oligomers will interact with the TiO_2 layer instead of having direct particle contact. This can be supported by the following UV-vis absorption experiments.

An affirmative way of confirming the viability of the application of melanin in DSSCs is to investigate the adsorption of the synthetic melanin onto the mesoporous TiO_2 surface. For this, a comparison was made between the UV-vis absorption spectra of the melanin in a DMSO/MeOH (1:19) solution and on a mesoporous TiO_2 film (see Fig. 1(f)). The melanin-sensitized mesoporous TiO_2 film was prepared by immersing TiO_2-fluorine-doped tin oxide (FTO) into the solution for 16 h. The corresponding light harvesting efficiencies can be seen in Fig. S1 (ESI†). As shown in Fig. 1(f), the melanin adsorbed on the mesoporous TiO_2 demonstrated light absorption ranging from 350 nm to 650 nm. It was compared to the simulated absorption spectrum obtained from theoretical calculations using MOLGW of a gas-phase melanin tetramer consisting of four semiquinone units, labeled as the "6H structure" and depicted in Fig. 1(b). This energetic minimum structure has been previously discussed in the works of Crescenci et al.[36] and Heppner et al.,[37] and is used here as a representative structure of many possible melanin structures (e.g., dimers or short linear chains of quinones/semiquinones/hydroquinones[38]), as the previous works have shown that this tetramer can be used as good approximation for simulating the electronic and optical properties of the material. In principle, other structures could be considered for simulation as well, as it has been shown that structures like isolated quinone monomers can also reproduce the optical properties of the material.[39] The simulated tetramer spectrum chosen here shows similar absorption to the thin-film melanin after normalization and shift correction to the first main maximum. However, the solution spectrum clearly differs from those of the corresponding thin film and simulation results, possibly due to solvation effects[40] and higher conjugated melanin instead of small oligomeric melanin being more dissolved, causing a shift in the spectrum. Based on the film and simulation data being similar, one can assume that the melanin adsorbed onto TiO_2 could be mostly of single-molecule or short-chain/oligomeric, e.g., tetrameric structures, suggesting that these small melanin structures contribute to the light-harvesting ability on the sensitized TiO_2 film instead of large agglomerated melanin particles. The simulation of the absorption spectrum also delivered the energetic locations of the HOMO (-6.17 eV) and LUMO (-3.40 eV) of the system with respect to vacuum. This gives an electronic gap of 2.77 eV, matching the HOMO–LUMO gap size of other dyes found in renewable, natural sources.[41] Furthermore, previous works have experimentally investigated the band locations and band gap size of eumelanin films using ultraviolet photoelectron spectroscopy (UPS) and inverse photoemission spectroscopy (IPES), and can be used to further confirm the validity of our calculations. Depending on the presence of DHI and DHICA units, HOMO–LUMO gap sizes between 1.7 eV and 2.5 eV were observed, also matching with the scale of our findings.[42]

Selecting redox electrolyte for melanin-DSSCs

To investigate melanin's capability for light-to-electric conversion within a DSSC, devices were prepared consisting of a photoelectrode, a counter electrode, and a redox electrolyte, structured in a sandwich cell. Our photoelectrodes were prepared by depositing a mesoporous TiO_2 layer onto FTO glass, followed by sensitization by immersion in a melanin solution (see Fig. S2 for a comparison of the TiO_2 photoanodes before and after the immersion process, ESI†). For the counter electrode, a platinum catalyst was deposited for utilizing an I^-/I^{3-} electrolyte, and poly(3,4-ethylenedioxythiophene) (PEDOT) was used for $Co^{(3+/2+)}(bpy)_3$ or $Cu^{(2+/1+)}(tmby)_2$ redox electrolytes. These electrodes were then assembled using a thermoplastic film, and the redox electrolyte was introduced into the internal
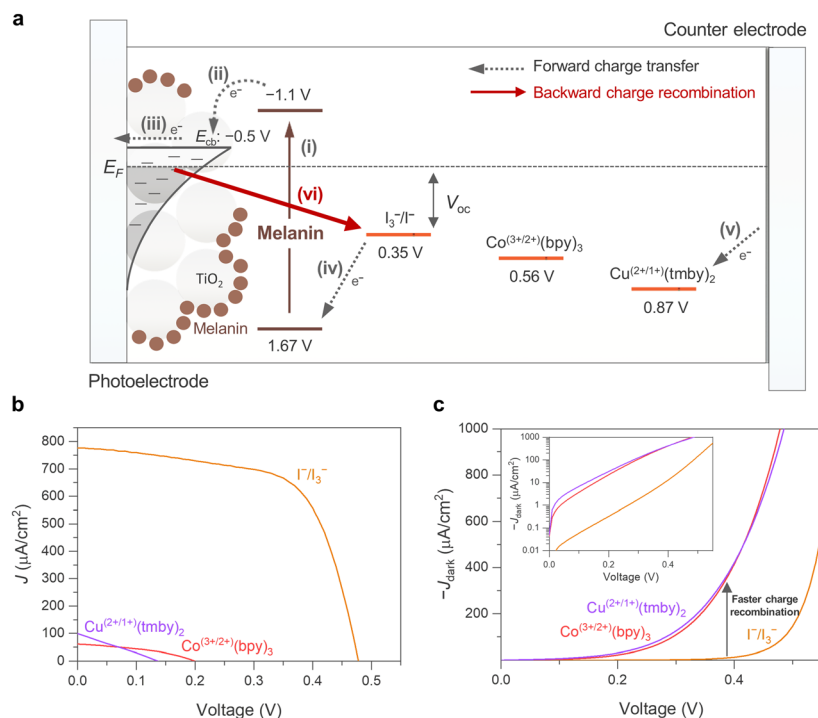
Fig. 2 Operational principle and performance investigation of melanin-DSSCs with varied electrolytes. (a) Energy level diagram showing the quasi-Fermi level (E_F) conduction band of the TiO$_2$, the HOMO and LUMO levels of melanin based on the calculation result, and the redox potentials of different electrolyte mediators, all referenced *versus* the normal hydrogen electrode (NHE). This diagram demonstrates the free energy differences driving forward charge transfer (dotted gray arrows) and backward charge recombination (solid red arrow). (b) J–V curves obtained under standard AM 1.5G sunlight at 100 mW cm^{-2} for melanin-DSSCs with different redox mediators, employing a mask to prevent the problem of overestimation. (c) Dark current curves of the melanin-DSSCs with different redox mediators, revealing highly accelerated charge recombination behavior at high-voltage bias in melanin-DSSCs with the metal-complex based mediators (Co$^{(3+/2+)}$(bpy)$_3$ and Cu$^{(2+/1+)}$(tmby)$_2$). The inset shows the same graph with a logarithmic scale, indicating the overall charge recombination characteristics.

cell space through a pre-drilled hole in the FTO glass. Detailed device assembly procedures can be found in the Materials and methods section.

Fig. 2(a) shows the operational principle of melanin-DSSCs as follows: (i) melanin anchored on TiO$_2$ absorbs incident light, generating photoexcited electron–hole pairs (photo-excitation). (ii) The photoexcited electrons in melanin are injected into the conduction band of TiO$_2$ (charge injection), oxidizing the melanin. (iii) These injected electrons then diffuse to the FTO glass through the TiO$_2$ transporting layer (charge transport). (iv) Simultaneously, the oxidized melanin is subsequently reduced by the redox mediator (charge regeneration), and the oxidized redox mediator diffuses to the counter electrode. (v) After diffusion, the oxidized redox mediator is reduced at the counter electrode. (vi) During device operation, a fraction of electrons recombines with the oxidized redox mediator at the TiO$_2$/electrolyte interface, reducing device performance (charge recombination).

The energetic position of melanin (Fig. 2(a)), with the HOMO (1.67 V *vs.* NHE) and LUMO (−1.1 V *vs.* NHE) obtained from the simulation results, provides a sufficiently free energy difference for charge injection (from the LUMO level of the melanin to the E_{cb} of TiO$_2$) and charge regeneration (from the redox levels of electrolytes to the HOMO level of the melanin).

We note that the well-known charge injection process (ii) described here is referred to as the "Type-I mechanism", typically utilized by sensitizers with hydroxyl groups.[43] Alternatively, some catechol moieties are known to facilitate charge injection *via* dye-to-TiO$_2$ transfer (DTCT, "Type-II mechanism") directly without leveraging the LUMO of the sensitizer.[43–45] Depending on the composition of sensitized melanin units, the specific charge injection mechanism may vary because of melanin's disordered structure. For instance, a very small fraction of distinct melanin monomers and dimers with catechol groups may utilize the Type-II mechanism for injection process.

Initially, we explored how electrolyte selection affects the power conversion efficiency (PCE) of melanin-DSSCs by measuring current density–voltage (J–V) curves under 100 mW cm^{-2} AM 1.5G conditions, as shown in Fig. 2(b). The PCE was determined using the equation:

$$\text{PCE} = \frac{J_{sc} V_{oc} \text{FF}}{P_{in}} \quad (1)$$

where J_{sc} is short-circuit current density, V_{oc} is open-circuit voltage, FF is fill factor, and P_{in} is incident light power. As indicated in Fig. 2(b) and Table S2 (ESI†), melanin-DSSCs using metal-complex based mediators (Co$^{(3+/2+)}$(bpy)$_3$ and

$Cu^{(2+/1+)}(tmby)_2$) showed negligible efficiencies (<0.005%), implying that these electrolytes are incompatible with the melanin energy conversion process. Only melanin-DSSCs with the I^-/I^{3-} electrolyte showed a PCE of 0.24%. Despite their thermodynamic compatibility with the HOMO level of melanin (Fig. 2(a)), the metal-complex mediators ($Co^{(3+/2+)}(bpy)_3$ and $Cu^{(2+/1+)}(tmby)_2$) exhibit significant kinetic limitations due to excessively high recombination rates observed in dark current analysis (Fig. 2(c)), leading to substantial backward losses that exceed forward light-to-electric conversion. It is well recognized that the metal-based redox mediators with one-electron transfers exhibit faster charge recombination kinetics than the iodine redox electrolyte.[46]

Validation of the melanin light-to-electric conversion

Having optimized the preparation of melanin-based DSSCs using an I^-/I^{3-} electrolyte, the utility of melanin in light-to-electric energy conversion was validated by comparison with unsensitized bare-TiO₂ devices as a control sample (Fig. 3(a)). The J–V characteristics, detailed in Fig. 3(a) and Table 1, revealed that while bare-TiO₂ DSSCs achieved a PCE of 0.056% (V_{oc} = 0.52 V, J_{sc} = 144 μA cm^{-2}, FF = 74.8%), the melanin-DSSCs exhibited a higher PCE of 0.24% (V_{oc} = 0.47 V, J_{sc} = 777 μA cm^{-2}, FF = 64.5%), primarily attributed to the increased J_{sc}. The contribution of the melanin to J_{sc} was quantified using the incident photon-to-electron conversion

Table 1 Photoelectrochemical parameters for DSSCs

Sample[a]	V_{oc} (V)	J_{sc} (μA cm^{-2})	FF (%)	PCE[b] (%)
Bare TiO₂	0.52 (0.51 ± 0.004)	144 (138 ± 3)	74.8 (75.0 ± 0.7)	0.056 (0.053 ± 0.002)
Melanin	0.47 (0.47 ± 0.004)	777 (716 ± 59)	64.5 (66.3 ± 1.7)	0.24 (0.22 ± 0.02)

[a] Measured under AM 1.5G 100 mW cm^{-2} sunlight. [b] The average and mean values ± standard deviations are shown, as obtained from 8 devices.

efficiency (IPCE) and integrated photocurrent values (J_{IPCE}). As depicted in Fig. 3(b), the bare-TiO₂ DSSCs were responsive in the 325 nm to 400 nm wavelength range, whereas the melanin-DSSCs displayed an extended photo-response up to 550 nm. These results confirm melanin's light-to-electric conversion, as previously indicated by the UV-vis spectroscopy analysis.

It is also crucial to clarify that the V_{oc} and FF in the melanin-DSSCs are lower than those in the bare-TiO₂ DSSCs. The V_{oc} is determined by the energy difference between the electron quasi-Fermi level of TiO₂ (E_F) and the energy level of the redox mediator of the iodine (I^-/I_3^-) electrolyte (Fig. 2(a)); thus, a decrease in E_F leads to a lower V_{oc}. This decrease in E_F is predominantly due to accelerated charge recombination kinetics between TiO₂ electrons and the oxidizing species in the electrolyte (e.g., I_3^- in the iodine electrolyte).[47] Similarly,
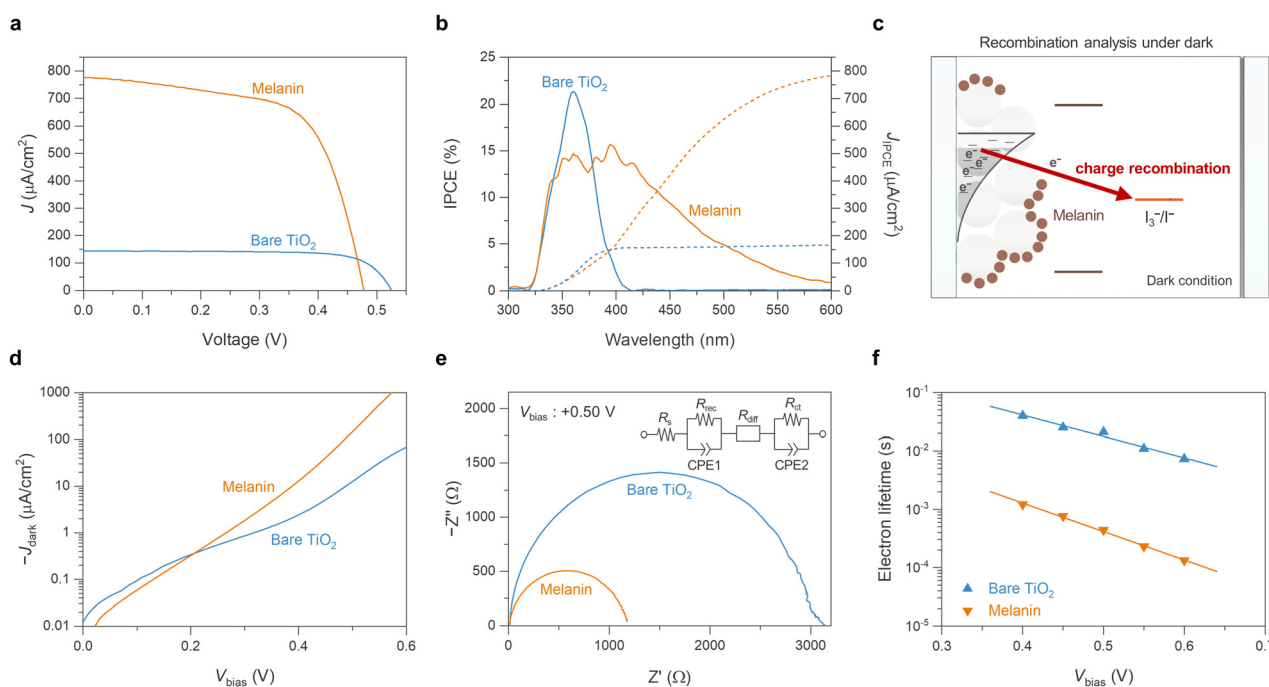

Fig. 3 Comparing the melanin-DSSC and the unsensitized bare-TiO₂ DSSC with charge recombination analysis in dark conditions. (a) J–V curves obtained under standard AM 1.5G sunlight at 100 mW cm^{-2}, employing a mask to prevent the issue of overestimation. (b) IPCE spectra (solid lines) measured in DC mode, along with the integrated photocurrent calculated from these IPCE spectra (J_{IPCE}, dotted lines). (c) Schematic representation of characterizing melanin-DSSCs in dark conditions, demonstrating the occurrence of charge recombination between TiO₂ and the electrolyte without any photoinduced charge transfer process. (d) Dark current curves of the DSSCs. (e) and (f) EIS analyses of the DSSCs: (e) features Nyquist plots with a corresponding equivalent circuit model obtained at a +0.50 V bias under dark conditions, and (f) shows the variations in electron lifetime as a function of V_{bias} ranging from +0.40 V to +0.60 V. The electron lifetime is determined using the equation $\tau = 1/(2\pi f_p)$, where f_p represents the peak frequency found in the mid-frequency region of the Bode phase plots (refer to Fig. S3, ESI†).

the decrease in FF is also mainly governed by the charge recombination rate as a function of applied bias.[48] In this context, melanin could play a role in enhancing the charge recombination kinetics. To investigate recombination kinetics, we conducted dark current characterization and electrochemical impedance spectroscopy (EIS) on both melanin-DSSCs and bare-TiO$_2$ DSSCs; note that charge recombination kinetics under dark conditions strongly depend on the interactions at the TiO$_2$ interface with the redox electrolyte.[49,50] As depicted in Fig. 3(d), the melanin-DSSCs exhibit more enhanced dark current characteristics than the bare-TiO$_2$ cells, indicating faster charge recombination. This observation is further supported through the EIS data, as shown in Fig. 3(e) and (f). The Nyquist plots in Fig. 3(e) reveal the smaller semi-circle in the mid-frequency range for melanin-DSSCs, indicating that melanin-DSSCs have a lower charge recombination resistance (R_{rec}) of 1156 Ω compared to 2976 Ω in bare-TiO$_2$ DSSCs. Additionally, Fig. 3(f) presents the electron lifetimes as a function of applied voltage, calculated from the Bode plot of EIS (Fig. S3, ESI†), displaying a shorter electron lifetime in the melanin-DSSCs due to accelerated charge recombination. One explanation for this could be the potential presence of the previously mentioned melanin semiquinone free radical units significantly affecting the chance of recombination events occurring.[7] Consequently, the reductions in V_{oc} and FF in the melanin-DSSCs are primarily attributed to accelerated charge recombination at the melanin-sensitized TiO$_2$ interface.

Understanding melanin electrochemistry in DSSCs

To further understand the electrochemical properties of the melanin-sensitized TiO$_2$ interface, the devices were investigated using intensity-modulated photovoltage spectroscopy (IMVS) and intensity-modulated photocurrent spectroscopy (IMPS). These small modulated-light perturbation techniques provide valuable insight into charge transport and recombination (Fig. 4(a)) in the TiO$_2$ photoanode as a function of incident light intensity (or electron concentration/photocurrent at that light intensity). As depicted in Fig. 4(b), IMPS measurements revealed a significantly lower electron transport time (τ_d) in the melanin-DSSCs compared to that of the bare-TiO$_2$ DSSCs. This suggests rapid transport of photoinjected electron carriers facilitated by melanin interacting with the TiO$_2$ layer. In contrast, Fig. 4(c) shows a decreased τ_e in the melanin-DSSCs, as observed in IMVS measurements, aligning with the findings from dark current and EIS analyses discussed earlier. Using the obtained results, the charge collection efficiency (η_{cc}), diffusion coefficient (D_n), and diffusion length (L_d), are calculated using eqn (2), (3) and (4), respectively:

$$\eta_{cc} = 1 - \frac{\tau_d}{\tau_e} \tag{2}$$

$$D_n \approx \frac{d^2}{2.35\tau_d} \tag{3}$$
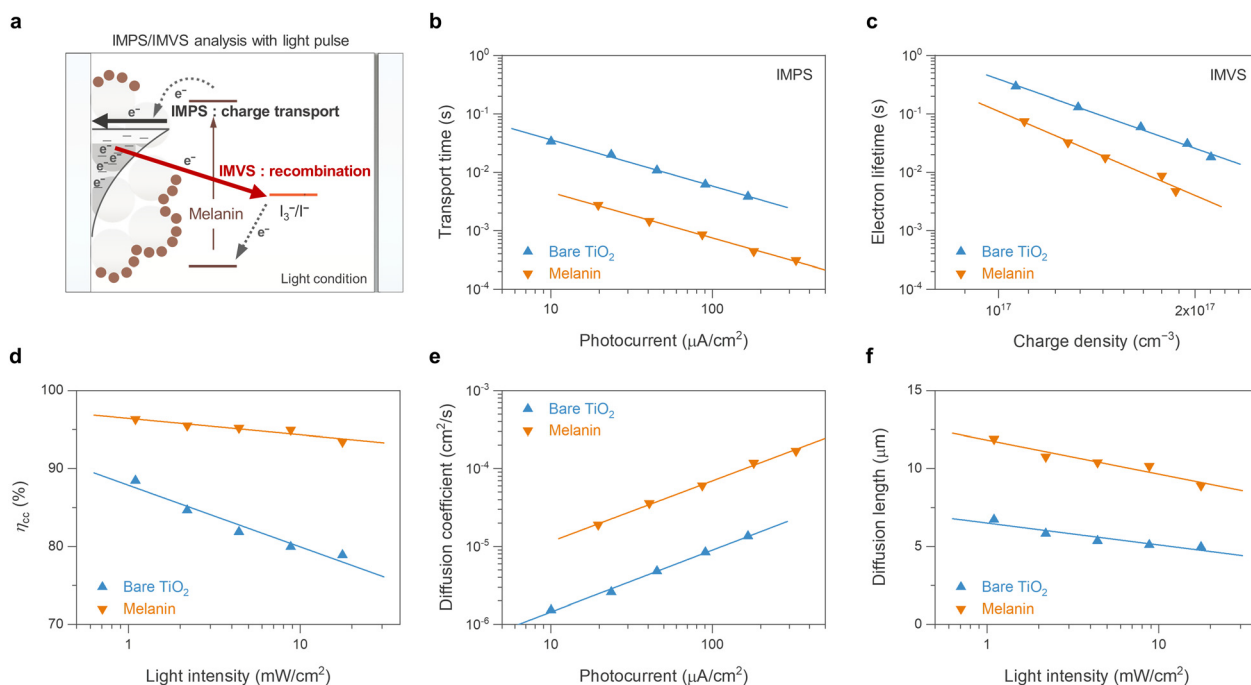
$$L_d = \sqrt{D_n\tau_e} \tag{4}$$

Fig. 4 Comparative IMPS/IMVS analysis for charge dynamics in melanin–DSSCs and bare TiO$_2$-DSSCs. (a) Schematic depicting the electron flow pathways during IMPS/IMVS analysis under light illumination, showing charge transport at short-circuit conditions (IMPS) and charge recombination at open-circuit conditions (IMVS). (b) Electron transport time, (c) electron lifetime, (d) charge collection efficiency, (e) diffusion coefficient, and (f) diffusion length of the mesoporous TiO$_2$ layer in both the melanin–DSSCs and bare TiO$_2$-DSSCs. For controlled IMPS/IMVS analysis, modulated monochromatic 435 nm (spectral halfwidth 30 nm) light was used together with an electrochemical workstation.

where d represents the mesoporous film thickness.[51,52] As shown in eqn (2), charge collection efficiency in dye-sensitized solar cells (DSSCs) represents the proportion of charge carriers successfully collected by the electrodes. Notably, despite the accelerated recombination kinetics, the melanin-based DSSCs exhibit higher charge collection efficiency, attributed to the enhanced charge transport effect (Fig. 4(d)). Furthermore, the calculated electron diffusion coefficient indicates the electron mobility while being transported in the TiO$_2$ layer. Melanin-DSSCs clearly show an improvement in the electron diffusion coefficient (Fig. 4(e)) and electron diffusion length (Fig. 4(f)) in TiO$_2$.

On the basis of the preceding analysis, it is proposed that the enhanced ionic interaction facilitated by the melanin anchored on the TiO$_2$/electrolyte interface is responsible for the observed phenomena. The potential porphyrin-like structure of melanin, containing carboxylates, aromatic amines, and quinone and catechol moieties, is well known for exhibiting strong cation interactions, including with lithium ions and other monovalent ions.[53,54] This behavior has been observed in both melanin and polydopamine-systems alike and is supported by theoretical calculations confirming metal-ion chelation both inside the porphyrin-like ring centres and at the catechol moieties.[55] The enhanced cation interaction contributes to the charge transport, which is considered an "ambipolar diffusion model". Specifically, at the TiO$_2$ interface surrounded by redox electrolyte with high ionic strength, the movement of electrons within the conduction band of TiO$_2$ is closely coupled with the diffusion of cations (*e.g.*, Li$^+$) in the electrolyte, ensuring electrical neutrality of the TiO$_2$/electrolyte interface.[56,57] Consequently, the enhanced diffusion of cations at the TiO$_2$ interface results in faster ambipolar charge transport of electrons within the conduction band of TiO$_2$. Furthermore, the accelerated charge recombination kinetics observed in melanin-DSSCs can be understood within the same context. The strong cation interaction at the TiO$_2$/electrolyte interface attracts anions such as I$_3^-$ to compensate for charges, resulting in their close proximity to the surface and thus accelerating charge recombination.[49] A graphical schematic of how the melanin recombination kinetics differ in DSSCs can be seen in Fig. S4 (ESI†). Similar observations of charge transport and recombination in DSSCs have been reported in previous studies, where the functional groups or donor parts of photosensitizers modify ion attraction at the TiO$_2$ surface.[58,59] This interpretation would also explain why melanin DSSCs are not working well with the metal-based electrolytes ((Co$^{(3+/2+)}$(bpy)$_3$) and (Cu$^{(2+/1+)}$(dmp)$_2$)) (Fig. 2), because melanin has a high affinity for the chelation of metal ions.

Long-term stability of melanin-DSSCs

The stability of the dye-TiO$_2$ interface is a central issue in utilizing natural or synthetic dyes in DSSCs. The catechol and quinone groups in melanin act as strong binding anchors on TiO$_2$, promoting a stable dye-TiO$_2$ interface in the redox electrolyte environment. Additionally, the catechol groups in melanin are known to contribute to its high electrochemical cycling stability due to their conjugated nature in the melanin

oligomers, as well as stabilization through control of the chelation of metal ions.[60] To assess the long-term stability of melanin-DSSCs, a light stability test employing a 1 sun LED solar simulator (wavelength range: 400–1100 nm) at room temperature (RT) was conducted. As illustrated in Fig. 5, the melanin-DSSCs exhibited high photo-stability, retaining 96% of the initial PCE value after 1000 hours. Specifically, the well-maintained J_{sc} of 103% implies the robust photochemical stability of both the structure of melanin and the melanin-sensitized TiO$_2$ interface under operational conditions. The observed decrease in V_{oc} (−11%) and the increase in FF (+5.0%) are likely due to changes in the interaction between iodine or triiodide and the dye-TiO$_2$/electrolyte interface during this period.[59,61] This result indicates that the melanin performs a stable light-to-electric conversion for a long period.

Considering the absence of UV exposure in our 1 sun stability tests and melanin being known for having a high potential for UV absorption, the logical next step was to investigate the UV stability of melanin-DSSCs.[62] These cells were exposed to a 365 nm UV lamp at an intensity of 1.80 mW cm^{-2} (wavelength range: 320–380 nm), comparable to the AM 1.5G solar spectrum, 300–400 nm range intensity of 1.37 mW cm^{-2}. Contrary to possible expectations of photo-degradation, surprisingly, 1000 hours of UV exposure resulted in an unexpected improvement in both J_{sc} and PCE by +84% and +73%, respectively (Fig. 5(b) and (d)), where the initial 530 hours showed a sharp increase, followed by a plateau. Also observed was a decrease in V_{oc} of −13% and an increase in FF of +8.6%, consistent with the 1 sun stability test results, indicating potential modifications in electrolyte interaction. Increased interaction of absorbing iodine species would accelerate surface charge recombination after aging, resulting in the change of V_{oc}.[59,61] The champion UV-treated cell (Fig. 5(e)) achieved a PCE of 0.42% (V_{oc} = 0.42 V, J_{sc} = 1475 μA cm^{-2}, FF = 68.2%), surpassing the untreated device (PCE = 0.24%, V_{oc} = 0.47 V, J_{sc} = 777 μA cm^{-2}, FF = 64.5%). Comparing their IPCE results (Fig. 5(f)) revealed that the UV-treated melanin-DSSCs not only exhibited improved quantum efficiency but also an extended photo-response up to 650 nm. Regarding the question of the origin of the J_{sc} enhancement, there are two further possibilities: (i) in the field of DSSCs, a few studies have suggested that prolonged light-soaking can improve J_{sc} due to changes in the dye arrangement on the TiO$_2$ surface and in the electrolyte interaction;[63,64] however, this appears unlikely in our case, considering the negligible change in J_{sc} observed during the more intense 1 sunlight stability test. (ii) The notable improvement under UV light exposure might originate from compositional and/or structural changes in melanin, which in turn may enhance light-harvesting and/or charge transfer properties. The expanded IPCE spectra support this scenario. For instance, the interaction of the melanin tetramer structure with abundant iodine species under UV light might lead to changes in its structural and/or photoelectrochemical properties. The inclusion of iodine species into conjugated organic polymers has been reported to result in a bathochromic shift of the absorption spectrum, which would correlate with
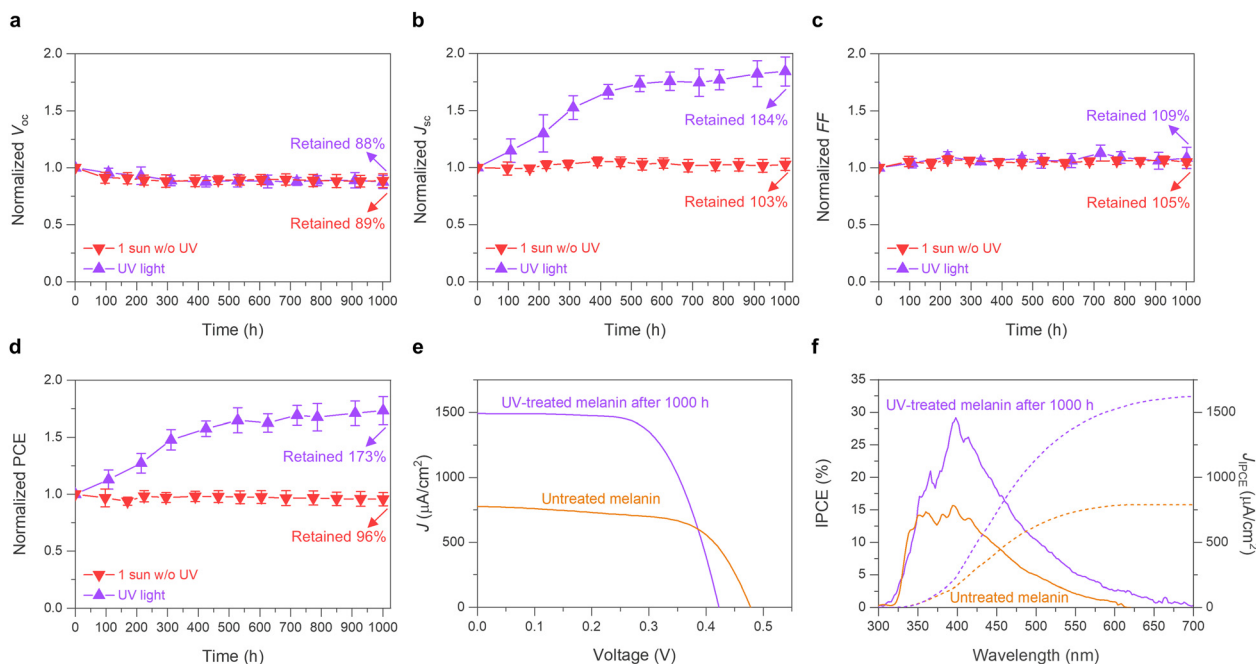
Fig. 5 Stability assessments of melanin–DSSCs under 1 sun and UV light conditions. This image shows the long-term stability of melanin–DSSCs through normalized parameters during 1000 hours light soaking, presenting (a) V_{oc}, (b) J_{sc}, (c) FF, and (d) PCE; the data are averaged across 10 cells, and error bars represent the standard deviations. The 1 sun stability test (red) was conducted using a 1 sun LED solar simulator and the UV stability test was conducted using a 365 nm UV lamp. The cells were stored at RT without additional temperature control. (e) and (f) Comparison of the champion cell before and after the 1000-hour UV stability test: (e) shows J–V curves under standard AM 1.5 G sunlight at 100 mW cm^{-2}, and (f) shows IPCE spectra (solid lines) alongside the integrated photocurrent calculated from these IPCE spectra (J_{IPCE}, dotted lines).

the increased performance until the maximum, where the incorporation of iodine would be saturated, explaining the following plateau of the data.[65] Another possible explanation could be that as observed previously in the literature, a significant enhancement of (semiquinone) radical ion concentration under UV light occurred over time, also affecting the rate of subsequent charge recombination.[66] These possibilities will be explored in more detail in future work. Measurements at 1 sun typically only heat up the sample for a maximum of about an additional 10 °C and the UV light exposure at the used low light intensities keeps the sample around RT. Coupled with the good thermal stability of melanin observed in the literature,[67,68] intense thermal degradation of the compounds used in the constructed devices can be excluded as the cause of these observed effects. Our long-term testing confirms the robust interface stability of melanin, comparing favorably with that of the most commonly used natural dyes in DSSCs.[69]

Conclusions

In this work, both the viability of using melanin as a sustainable natural dye in DSSC devices, and potential shortcomings to overcome in future optimizations of this system were demonstrated and explained. Using a TiO$_2$ substrate and an iodine-based electrolyte, process-optimized DSSCs with high cycling stability and an efficiency of 0.24% before and 0.42% after treatment with UV-light, higher than previous works

employing synthetic melanin, have been obtained. The produced melanin films were shown to have a high absorption range in the UV-vis region, comparable to the theoretical maximum obtained from computational studies. The short circuit current increasing over long periods of UV-exposure might correlate to potential changes in the melanin structure over time when interacting with the iodine electrolyte. The enhanced current output upon UV-exposure is a novel property not commonly observed for comparable polymer compounds with less hierarchical structuring than melanin. Spectroscopic and microscopic analyses indicated reasons for good melanin–TiO$_2$ interaction; the small oligomer size, the presence of the porphyrin-like tetramer centres, and quinone as well as catechol moieties leading to good surface ion interaction. While these properties result in a high operating stability of the system, the main limitations observed for the melanin DSSCs were the lack of flexibility in electrolyte selection and the high recombination rate observed from IMPS and IMVS studies, potentially affected by the presence of semiquinone free radicals. Thus, future work should employ either chemical modification of melanin by the introduction of functional groups that can affect the charge transfer kinetics through electron-withdrawing moieties, or the use of multi-dye systems to carefully engineer the band gap of the system to minimize the chance for recombination, to fully unlock the potential of using melanin as a natural dye in DSSC applications.[70] The sustainability aspect could be further explored by employing melanin from different natural origins like fungi, insects, or biological waste.[71–73]

In summary, this work has successfully reintroduced melanin into the picture of natural dyes for DSSCs by process-optimizing the constructed devices and shedding light on their potential applications in light-to-electric conversion.

Materials and methods

Materials and reagents

Synthetic melanin (M8631) synthesized from tyrosine by oxidation with hydrogen peroxide was obtained from Sigma-Aldrich. Deionized water (MQ) was used in a filtered state from a Milli-q A10 Biocel water purification system with Millipak Express 20 filters purchased from Merck Millipore. Silica wafers, methanol (reagent grade), and DMSO (reagent grade) were bought from Sigma-Aldrich and double-sided conductive carbon tape was obtained from Fisher Scientific. Further details on the used chemicals and materials are described in the ESI.†

Preparation of devices

Melanin-based DSSCs were prepared consisting of a sensitized TiO_2 photoanode, a redox electrolyte, and a Pt-coated counter electrode. A photograph of the prepared devices can be seen in Fig. S5 (ESI†). The TiO_2 photoelectrodes were prepared by employing the TiO_2 paste (18NR-AO) on cleaned fluorine-doped tin oxide (FTO) glass using a screen-printing method (4 mm × 4 mm). Subsequently, the sensitizing with synthetic melanin was performed by immersing the film into the synthetic melanin solution (10 mg in a 20 mL mixture of DMSO and MeOH (1 : 19, vol : vol)) for 16 h. The Pt-coated counter electrodes were prepared by using a brushing method, applying a 10 mM $H_2PtCl_6\cdot6H_2O$ (~40% Pt, Sigma-Aldrich) ethanol solution onto cleaned FTO glass. The prepared photoanode and the counter electrode were assembled into a sandwich-type cell and sealed with a 25 μm-thick thermoplastic sealing film (Meltonix 1170-25). The interspace of the sandwich cell was filled with a redox electrolyte using a vacuum filling technique. Detailed preparation procedures can be found in the ESI.†

Material characterization

Raman experiments were performed at RT in a confocal set-up using a LabRAM HR Raman Instrument (Horiba) with a 514.5 nm Argon ion laser. The bulk melanin powder samples were placed onto rinsed glass slides and observed using a 100× objective lens. Employing a D 0.3 filter while using an acquisition time of 15 s, the Raman spectra were recorded from 3500 nm to 100 nm. The gathered data was analyzed using the Origin 2022 and LabSpec 6 software.

For the SEM investigations, melanin was dispersed in MQ and sonicated using a probe-sonicator at 6 Horn, 200 W, T-on = 2.0, and T-off = 1.0 inside a 0 °C ice bath for 10 min to produce a powder that attaches easily to the selected substrate and was drop-cast on a silica wafer. The wafer was dried under a static vacuum overnight using a desiccator with sodium sulfate as a drying agent. Using double-sided carbon tape, the wafer was then ground onto the stub used for SEM and coated with Pt for

a few nm, in order to lower charging side effects during imaging. The sample microstructures and morphology were analyzed with a field-emission scanning electron microscope (FE-SEM 6240F, JEOL) using a relatively low value (5.0 kV) beam energy in order to prevent beam damage of the sample. The images produced were recorded at different magnifications between 150k and 10k.

Computational methods

GW-BSE calculations were performed using MOLGW version 3.2.[74] First, a G_6W_0 calculation was performed, directly followed by a BSE (Bethe–Salpeter equation) calculation.[75–77] Both were performed at the BHLYP/cc-pVDZ(-RI) level of theory. For all calculations, the frozen core approximation was applied and the melanin gas phase "6 H structure" tetramer described in previous works, consisting of four semiquinone units, was used as an approximation for the melanin structure, giving the absorption energy of the system at different wavelengths that can be converted into a simulated UV-vis spectrum.[36,37] The spectrum was normalized to 1 at the first overall maximum and shifted to the location of that peak in the empirical data to accommodate for solvation effects and ensure comparability between the data. The plot of the raw simulated data can be found in Fig. S6 (ESI†).

Electrochemical characterization of the DSSC devices

The performance of the fabricated DSSC devices was measured using the PEC-L01 (Peccell) solar spectrum simulator system. Before measurement, the system was calibrated to standard AM 1.5G conditions using a certified Si reference cell, PEC-SI01 (Peccell). The J–V curves of the solar cells were obtained by scanning voltages from −0.1 to 0.6 V at a scan rate of 50 mV/s with incremental voltage steps of 10 mV. For IPCE investigations, the PEIPCE 120 system (HS Technologies) with a 150 W xenon arc lamp was employed. The IPCE of the solar cells was measured under the AM 1.5G condition, which was calibrated using the PEC-SI02 (Peccell) Si reference cell. EIS data were measured at a forward bias of 0.50 V under dark conditions. The Nyquist plots were obtained from EIS measurements with 10 mV of perturbation amplitude within a frequency from 10^6 to 10^{-1} Hz. IMPS/IMVS analyses were conducted using an electrochemical workstation (ZENNIUM XPOT, ZAHNER-elektrik GmbH & Co. KG), equipped with a light-emitting diode and its corresponding control system. Further descriptions of the photoelectrochemical measurements are found in the ESI.†

Author contributions

All authors listed have made a substantial, direct, and intellectual contribution to the work and approved it for publication. N.A.-S., J.-H. P., and S. R. K. contributed equally and share first authorship. They conceived the original work under the main supervision of P. S. L. and T.-H. K. N. A.-S. advised on experimental planning and performed microscopic and spectroscopic characterization. J.-H. P. and S. R. K. performed absorption

spectroscopy, as well as device preparation, and photoelectrochemical testing and analysis with the assistance of S. Y. Y. F. H. advised by T. B. performed theoretical calculations and correlated analysis. N. A.-S. and J.-H.P. with the help of S. R. K. wrote the original draft; T. B., P. S. L., and T.-H. K. reviewed and edited the manuscript.

Data availability

The data supporting this article, including unedited simulation data and exact fabrication procedures for reproducing measurements, have been included as part of the ESI.†

Conflicts of interest

There are no conflicts of interest to declare.

Acknowledgements

References

1 M. d'Ischia, K. Wakamatsu, F. Cicoira, E. Di Mauro, J. C. Garcia-Borron, S. Commo, I. Galván, G. Ghanem, K. Kenzo, P. Meredith, A. Pezzella, C. Santato, T. Sarna, J. D. Simon, L. Zecca, F. A. Zucca, A. Napolitano and S. Ito, *Pigm. Cell Melanoma Res.*, 2015, **28**, 520–544.

2 M. d'Ischia, K. Wakamatsu, A. Napolitano, S. Briganti, J.-C. Garcia-Borron, D. Kovacs, P. Meredith, A. Pezzella, M. Picardo, T. Sarna, J. D. Simon and S. Ito, *Pigm. Cell Melanoma Res.*, 2013, **26**, 616–633.

3 A. B. Mostert, S. B. Rienecker, M. Sheliakina, P. Zierep, G. R. Hanson, J. R. Harmer, G. Schenk and P. Meredith, *J. Mater. Chem. B*, 2020, **8**, 8050–8060.

4 P. Kumar, E. D. Mauro, S. Zhang, A. Pezzella, F. Soavi, C. Santato and F. Cicoira, *J. Mater. Chem. C*, 2016, **4**, 9516–9525.

5 D. Zhang, S. M. Lanier, J. A. Downing, J. L. Avent, J. Lum and J. L. McHale, *J. Photochem. Photobiol., A*, 2008, **195**, 72–80.

6 R. Xu, A. Gouda, M. F. Caso, F. Soavi and C. Santato, *ACS Omega*, 2019, **4**, 12244–12251.

7 A. B. Mostert, *Chem. Phys.*, 2021, **546**, 111158.

8 M. Sugumaran, J. Evans, S. Ito and K. Wakamatsu, *Int. J. Mol. Sci.*, 2020, **21**, 7321.

9 A. Pezzella, O. Crescenzi, A. Natangelo, L. Panzella, A. Napolitano, S. Navaratnam, R. Edge, E. J. Land, V. Barone and M. D'Ischia, *J. Org. Chem.*, 2007, **72**, 1595–1603.

10 M. d'Ischia, A. Napolitano, A. Pezzella, P. Meredith and M. Buehler, *Angew. Chem., Int. Ed.*, 2020, **59**, 11196–11205.

11 S. Meng and E. Kaxiras, *Biophys. J.*, 2008, **94**, 2095–2105.

12 M. Salomäki, L. Marttila, H. Kivelä, T. Ouvinen and J. Lukkari, *J. Phys. Chem. B*, 2018, **122**, 6314–6327.

13 K. A. Motovilov, V. Grinenko, M. Savinov, Z. V. Gagkaeva, L. S. Kadyrov, A. A. Pronin, Z. V. Bedran, E. S. Zhukova, A. B. Mostert and B. P. Gorshunov, *RSC Adv.*, 2019, **9**, 3857–3867.

14 K. Wang, Y. Hou, B. Poudel, D. Yang, Y. Jiang, M. G. Kang, K. Wang, C. Wu and S. Priya, *Adv. Energy Mater.*, 2019, **9**, 1901753.

15 S. Meng and E. Kaxiras, *Biophys. J.*, 2008, **95**, 4396–4402.

16 M. Yang, T. Chu, J. Shi, J. Zhang, Y. Zhang and L. Wang, *Colloids Surf., A*, 2022, **632**, 127786.

17 P. Meredith and T. Sarna, *Pigm. Cell Res.*, 2006, **19**, 572–594.

18 A. B. Mostert, S. B. Rienecker, C. Noble, G. R. Hanson and P. Meredith, *Sci. Adv.*, 2018, **4**, eaaq1293.

19 C. Silva, A. Santos, R. Salazar, C. Lamilla, B. Pavez, P. Meza, R. Hunter and L. Barrientos, *Sol. Energy*, 2019, **181**, 379–385.

20 H. J. Nam, B. Kim, M. J. Ko, M. Jin, J. M. Kim and D.-Y. Jung, *Chem. – Eur. J.*, 2012, **18**, 14000–14007.

21 N. A. Ludin, A. M. Al-Alwani Mahmoud, A. Bakar Mohamad, A. A. H. Kadhum, K. Sopian and N. S. Abdul Karim, *Renewable Sustainable Energy Rev.*, 2014, **31**, 386–396.

22 J. Gong, J. Liang and K. Sumathy, *Renewable Sustainable Energy Rev.*, 2012, **16**, 5848–5860.

23 A. Kay and M. Graetzel, *J. Phys. Chem.*, 1993, **97**, 6272–6277.

24 G. Calogero, J.-H. Yum, A. Sinopoli, G. Di Marco, M. Grätzel and M. K. Nazeeruddin, *Sol. Energy*, 2012, **86**, 1563–1575.

25 A. Mbonyiryivuze, I. Omollo, B. D. Ngom, B. Mwakikunga, S. M. Dhlamini, E. Park and M. Maaza, *Phys. Mater. Chem.*, 2015, **3**, 1–6.

26 N. M. Dimitrijevic, O. G. Poluektov, Z. V. Saponjic and T. Rajh, *J. Phys. Chem. B*, 2006, **110**, 25392–25398.

27 Z. Tachan, I. Hod and A. Zaban, *Adv. Energy Mater.*, 2014, **4**, 1301249.

28 S. Ferrere and B. A. Gregg, *J. Phys. Chem. B*, 2001, **105**, 7602–7605.

29 E. S. Falsgraf, *Pomona Senior Theses*, 2012, 61.

30 R. M. Haywood, M. Lee and C. Linge, *J. Photochem. Photobiol., B*, 2006, **82**, 224–235.

31 V. Capozzi, G. Perna, A. Gallone, P. F. Biagi, P. Carmone, A. Fratello, G. Guida, P. Zanna and R. Cicero, *J. Mol. Struct.*, 2005, **744–747**, 717–721.

32 V. Varade, G. V. Honnavar, P. Anjaneyulu, K. P. Ramesh and R. Menon, *J. Phys. D: Appl. Phys.*, 2013, **46**, 365306.

33 W. Q. Wang, H. Y. Yue, Z. M. Yu, S. Huang, S. S. Song, X. Gao, E. H. Guan, H. J. Zhang and Z. Wang, *Ionics*, 2019, **25**, 2835–2843.

34 E. Harki, T. Talou and R. Dargent, *Food Chem.*, 1997, **58**, 69–73.

35 N. Al-Shamery, T. Benselfelt and P. S. Lee, *ACS Appl. Mater. Interfaces*, 2023, **15**, 25966–25979.

36 O. Crescenzi, M. D'Ischia and A. Napolitano, *Biomimetics*, 2017, **2**, 21.

37 F. Heppner, N. Al-Shamery, P. S. Lee and T. Bredow, *Mater. Adv.*, 2024, **5**, 5251–5259.

38 C.-T. Chen, F. J. Martin-Martinez, G. S. Jung and M. J. Buehler, *Chem. Sci.*, 2017, **8**, 1631–1641.

39 X. Wang, L. Kinziabulatova, M. Bortoli, A. Manickoth, M. A. Barilla, H. Huang, L. Blancafort, B. Kohler and J.-P. Lumb, *Nat. Chem.*, 2023, **15**, 787–793.

40 R. Tomar, L. Bernasconi, D. Fazzi and T. Bredow, *J. Phys. Chem. A*, 2023, **127**, 9661–9671.

41 N. N. A. Hamid, S. Suhaimi and N. M. Yatim, *AIP Conf. Proc.*, 2018, **1972**, 030009.

42 D. Niyonkuru, A. Carrière, R. Ambrose, A. Gouda, M. Reali, A. Camus, A. Pezzella, I. Hill and C. Santato, *J. Chem. Technol. Biotechnol.*, 2022, **97**, 837–843.

43 Y. Ooyama, M. Kanda, K. Uenaka and J. Ohshita, *Chem. Phys. Chem.*, 2015, **16**, 3049–3057.

44 F. K. Asiam, M. M. Rahman, A. K. Kaliamurthy, S. Muthu, B. Yadagiri, H. C. Kang, C. Chen, K. Yoo and J.-J. Lee, *J. Phys. Chem. C*, 2023, **127**, 3928–3939.

45 F. Kwaku Asiam, A. Kumar Kaliamurthy, M. Mahbubur Rahman, B. Yadagiri, C. Chen, H. Cheol Kang, M. Sadiq, J. Ryu, A. Ewusi Mensah, M. Zain Qamar, K. Yoo and J.-J. Lee, *Coord. Chem. Rev.*, 2024, **514**, 215908.

46 S. Kambe, S. Nakade, T. Kitamura, Y. Wada and S. Yanagida, *J. Phys. Chem. B*, 2002, **106**, 2967–2972.

47 P. R. F. Barnes, A. Y. Anderson, M. Juozapavicius, L. Liu, X. Li, E. Palomares, A. Forneli and B. C. O'Regan, *Phys. Chem. Chem. Phys.*, 2011, **13**, 3547–3558.

48 H. J. Snaith and L. Schmidt-Mende, *Adv. Mater.*, 2007, **19**, 3187–3200.

49 M. Miyashita, K. Sunahara, T. Nishikawa, Y. Uemura, N. Koumura, K. Hara, A. Mori, T. Abe, E. Suzuki and S. Mori, *J. Am. Chem. Soc.*, 2008, **130**, 17874–17881.

50 D.-H. Roh, J.-H. Park, H.-G. Han, Y.-J. Kim, D. Motoyoshi, E. Hwang, W.-H. Kim, J. I. Mapley, K. C. Gordon, S. Mori, O.-H. Kwon and T.-H. Kwon, *Chem*, 2022, **8**, 1121–1136.

51 J. Van De Lagemaat and A. J. Frank, *J. Phys. Chem. B*, 2001, **105**, 11194–11205.

52 J.-H. Park, D. G. Nam, B.-M. Kim, M. Y. Jin, D.-H. Roh, H. S. Jung, D. H. Ryu and T.-H. Kwon, *ACS Energy Lett.*, 2017, **2**, 1810–1817.

53 Z. Tian, W. Hwang and Y. J. Kim, *J. Mater. Chem. B*, 2019, **7**, 6355–6361.

54 T. Sun, Z. J. Li, H. G. Wang, D. Bao, F. L. Meng and X. B. Zhang, *Angew. Chem., Int. Ed.*, 2016, **55**, 10662–10666.

55 Y. J. Kim, A. Khetan, W. Wu, S.-E. Chun, V. Viswanathan, J. F. Whitacre and C. J. Bettinger, *Adv. Mater.*, 2016, **28**, 3173–3180.

56 N. Kopidakis, K. D. Benkstein, J. Van De Lagemaat and A. J. Frank, *J. Phys. Chem. B*, 2003, **107**, 11307–11315.

57 D. Nistér, K. Keis, S.-E. Lindquist and A. Hagfeldt, *Sol. Energy Mater. Sol. Cells*, 2002, **73**, 411–423.

58 J. Yang, P. Ganesan, J. Teuscher, T. Moehl, Y. J. Kim, C. Yi, P. Comte, K. Pei, T. W. Holcombe, M. K. Nazeeruddin, J. Hua, S. M. Zakeeruddin, H. Tian and M. Grätzel, *J. Am. Chem. Soc.*, 2014, **136**, 5722–5730.

59 J.-H. Park, U.-Y. Kim, B.-M. Kim, W.-H. Kim, D.-H. Roh, J. S. Kim and T.-H. Kwon, *ACS Appl. Energy Mater.*, 2019, **2**, 4674–4682.

60 D. Vonlanthen, P. Lazarev, K. A. See, F. Wudl and A. J. Heeger, *Adv. Mater.*, 2014, **26**, 5095–5100.

61 P. Wang, L. Yang, H. Wu, Y. Cao, J. Zhang, N. Xu, S. Chen, J.-D. Decoppet, S. M. Zakeeruddin and M. Grätzel, *Joule*, 2018, **2**, 2145–2153.

62 S. Ito, K. Wakamatsu and T. Sarna, *Photochem. Photobiol.*, 2018, **94**, 409–420.

63 J. Gao, A. M. El-Zohry, H. Trilaksana, E. Gabrielsson, V. Leandri, H. Ellis, L. D'Amario, M. Safdari, J. M. Gardner, G. Andersson and L. Kloo, *ACS Appl. Mater. Interfaces*, 2018, **10**, 26241–26247.

64 L. Cabau, L. Pellejà, J. N. Clifford, C. V. Kumar and E. Palomares, *J. Mater. Chem. A*, 2013, **1**, 8994.

65 J. Sun, A. M. S. Riel and O. B. Berryman, *New J. Chem.*, 2018, **42**, 10489–10492.

66 T. Sarna and R. C. Sealy, *Arch. Biochem. Biophys.*, 1984, **232**, 574–578.

67 O. F. Restaino, P. Manini, T. Kordjazi, M. L. Alfieri, M. Rippa, L. Mariniello and R. Porta, *Microorganisms*, 2024, **12**, 297.

68 S. S. Sawhney, *Thermochim. Acta*, 1994, **247**, 377–380.

69 F. Kabir, S. Manir, M. M. H. Bhuiyan, S. Aftab, H. Ghanbari, A. Hasani, M. Fawzy, G. L. T. De Silva, M. R. Mohammadzadeh, R. Ahmadi, A. Abnavi, A. M. Askar and M. M. Adachi, *Sustainable Energy Technol. Assess.*, 2022, **52**, 102196.

70 M. Akhtaruzzaman, M. Shahiduzzaman, V. Selvanathan, K. Sopian, M. I. Hossain, N. Amin and A. K. M. Hasan, *Appl. Mater. Today*, 2021, **25**, 101204.

71 A. N. Tran-Ly, J. Ribera, F. W. M. R. Schwarze, M. Brunelli and G. Fortunato, *Sustainable Mater. Technol.*, 2020, **23**, e00146.

72 E. Kim, C.-Y. Chen, J. W. Phua, A. Napolitano, W. E. Bentley and G. F. Payne, *J. Phys. Chem. C*, 2023, **127**, 19979–19994.

73 A. E. Aghajanyan, A. A. Hambardzumyan, E. V. Minasyan, A. H. Tsaturyan, A. M. Paloyan, S. V. Avetisyan, A. S. Hovsepyan and A. S. Saghyan, *Eur. Food Res. Technol.*, 2022, **248**, 485–495.

74 F. Bruneval, T. Rangel, S. M. Hamed, M. Shao, C. Yang and J. B. Neaton, *Comput. Phys. Commun.*, 2016, **208**, 149–161.

75 A. D. Becke, *J. Chem. Phys.*, 1993, **98**, 1372–1377.

76 T. H. Dunning, Jr., *J. Chem. Phys.*, 1989, **90**, 1007–1023.

77 D. E. Woon and T. H. Dunning, Jr., *J. Chem. Phys.*, 1993, **98**, 1358–1371.